JOURNAL OF THERMOPHYSICS AND HEAT TRANSFER
Vol. 16, No. 1, January–March 2002

Unified Calculation of Hypersonic Flowfield for a Reentry Vehicle

Toshiyuki Suzuki,* Michiko Furudate,† and Keisuke Sawada‡
Tohoku University, Sendai 980-8579, Japan

A unified computational fluid dynamics (CFD) method is developed that integrates numerical methods for solving specific problems related to aerodynamic heating phenomena and ablative heatshield. With the use of this unified CFD code, trajectory-based analysis on the aerodynamic heating environment for the MUSES-C superorbital reentry capsule is conducted. Converged solutions can be obtained by loosely coupling the CFD code and the charring materials ablation code within a few iterations. The results show that the wall surface temperature in the downstream region is significantly elevated by the effect of turbulence due to ablation product gas. Wall temperature as well as the recession rate at the stagnation point along the entry trajectory is found to duplicate well the existing predictions.

Nomenclature

A^+ = constant, 26
d = mixing length, m
E = total energy per unit volume, J/m^3
E_v = vibrational–electron–electronic energy per unit volume, J/m^3
J_i = reaction rate, mol/(m$^2 \cdot$ s)
k = Boltzmann constant, 1.3806×10^{-16} erg/K
k_{wi} = surface reaction velocity, m/s
M_s = molecular weight of species s, kg/kmol
$\dot{m}_p$ = pyrolysis gas injection rate, kg/(m$^2 \cdot$ s)
n_s = number density of species s, cm^{-3}
$\boldsymbol{Q}$ = vector of conserved quantities
T = translational-rotational temperature, K
T_v = vibrational–electron–electronic temperature, K
u = velocity component in x direction, m/s
v = velocity component in y direction, m/s
y^+ = nondimensional wall coordinate
α_i = surface reaction probability
γ_s = concentration of species s, mol/kg
ε = void fraction
κ_λ = absorption coefficient at given wavelength including stimulated emission, cm^{-1}
μ_t = eddy viscosity, N $\cdot$ s/m^2
ρ_s = density of species s, kg/m^3
$\tilde{\rho}_s$ = elemental density of element s, kg/m^3
σ_λ = absorption cross section at given wavelength, cm^2
χ = von Kármán constant, 0.4
ω = vorticity, s^{-1}

Subscripts

BL = Baldwin–Lomax turbulence model[22]
E = equilibrium
i = reaction index
inj = injection flow from the wall surface
Park = Park's injection-induced turbulence model[5]
p = pyrolysis gas
w = wall

Introduction

LESSONS that can be learned from past planetary missions such as the Pioneer-Venus probes[1] and the Galileo probe[2] are really important in designing heatshields of future space vehicles. The flight data obtained during the reentry phase of Apollo return capsules are also extremely valuable.

Past attempts for reproducing the flight data in the entry flights were summarized by Park.[3] He pointed out that the higher temperature appeared near the frustum edge of the Pioneer-Venus probe vehicles could be caused by early transition of the boundary layer due to an ablation product gas. Promotion of turbulence due to spalled particles from the heatshield and nonequilibrium radiation of carbonaceous species in the shock layer could also be the cause.

The flight data obtained during the entry of the Galileo probe vehicle into the Jovian atmosphere also indicated substantial differences from preflight predictions. Although radiative heating was dominant in this case, the flight data analysis indicated that the char layer was thinner at the stagnation region and far thicker at the frustum region than that of the preflight predictions.[4] Therefore, the design methodology of ablative heatshields established so far in the United States obviously has a room for further improvements.

Ablation phenomena of heatshields involve complicated physics that make the prediction quite difficult. However, a simpler physical model that is suitable for explaining a specific problem can fail to give an overall description of the problem. Therefore, the only viable method for accurate prediction of ablation phenomena seems to be to account for various aspects of the problem simultaneously and, thus, to combine various computer codes for corresponding specific parts of the ablation phenomena.

For the higher heating rate probably caused by the earlier transition of the boundary layer, Park conjectured that the injected pyrolysis gas was already turbulent and had an increased heating rate. He developed a turbulence model based on the conventional mixing-length theory for characterizing the eddy viscosity of the injected pyrolysis gas at the stagnation point.[5] Ahn et al. applied this model to the entire surface of the Pioneer-Venus prove vehicle,[6] and they partially explained the observed higher temperature in the downstream region numerically.

In the sequel work of Izawa and Sawada,[7] a new implementation of Park's turbulence model was first developed to show an improved agreement with the corresponding data. With this new implementation method, the aerodynamic heating problem of the Pioneer-Venus probe vehicle was revisited[8] by combining a nonequilibrium thermochemical CFD code and a charred materials ablation (CMA) code.[9] A consistent boundary condition at the wall was accomplished by loosely coupling these codes iteratively along the flight trajectory. The temperature rise in the ablative heatshield at the

---

Presented as Paper 2001-0980 at the AIAA 39th Aerospace Sciences Meeting, Reno, NV, 8–11 January 2001; received 5 March 2001; revision received 4 October 2001; accepted for publication 4 October 2001. Copyright © 2001 by the American Institute of Aeronautics and Astronautics, Inc. All rights reserved. Copies of this paper may be made for personal or internal use, on condition that the copier pay the $10.00 per-copy fee to the Copyright Clearance Center, Inc., 222 Rosewood Drive, Danvers, MA 01923; include the code 0887-8722/02 $10.00 in correspondence with the CCC.

*Graduate Student, Department of Aeronautics and Space Engineering.

†Graduate Student, Department of Aeronautics and Space Engineering. Student Member AIAA.

‡Professor, Department of Aeronautics and Space Engineering. Senior Member AIAA.

frustum region was well reproduced, although several assumptions, such as to give the same stagnation radiative heat flux value over the entire surface, were made.

For the possible radiative heating, accurate prediction of the heat flux is only possible when flowfield is fully coupled with radiative heat transfer. A detailed line-by-line calculation of radiative intensity, however, requires prohibitively large computing time to obtain radiative heat flux values. Even the multiband model is considered to be too time consuming for fully coupled calculation of strongly radiating flowfield.

Recently, Sakai et al.[10] developed a radiation model, the Planck–Rosseland–gray (PRG) model, for reducing computing time in the radiation calculation. With the aid of the PRG model, a fully coupled calculation of the radiation-dominated flowfield has been shown to be feasible. Furthermore, the recent work of Tsuru and Sawada[11] showed that an implicit integration of the flow equations using the lower-upper symmetric Gauss–Seidel algorithm could give converged solutions for radiation dominated flowfield, even if the radiative heat flux term was integrated explicitly. Because of the explicit treatment of the radiative source term, not only the computing time but also the memory size needed for such calculation is substantially reduced. Sakai and Sawada showed that the nonequilibrium thermochemical CFD code could also be combined with the PRG model to give a strongly radiating nonequilibrium flowfield.[12] Therefore, it seems possible now to further combine the CFD codes for predicting convective heating and those for radiative heating, to give a unified approach that can potentially give an accurate solution of the flowfield involving ablation phenomena.

The ultimate aim of the present study is, thus, to integrate the hitherto developed numerical methods in our group for specific problems related to ablative heatshield and aerodynamic heating phenomena and to see whether reliable solutions that are needed for designing an ablative heatshield can be obtained. The flow features considered in the unified code will be 1) thermochemical nonequilibrium for high-temperature air including carbonaceous species, 2) thermal response of ablative heatshield using a CMA code, 3) injection-induced turbulence model, 4) fully coupled flowfield with radiative heat transfer, 5) shape change of heatshield due to recession, and 6) the effect of spalled particles from the heatshield.

Toward this goal, the present study considers flow features 1–3 just listed and makes a trajectory-based analysis on the aerodynamic heating environment for the MUSES-C superorbital reentry capsule. In this study, the radiative heat flux transferred to the wall surface is computed by the tangent-slab approximation with using a multiband method and is only used as the boundary condition in the CMA code. Thus, the flowfield is indirectly coupled with radiation through the change in the property of ablation product gas. A fully coupled calculation with radiative heat transfer, as well as recession of the heatshield (features 4 and 5), will be considered in a separate paper. Inclusion of effect of spallation, however, seems to need further effort.

Numerical Methods

The governing equations are the Navier–Stokes equations for an axisymmetric flowfield, consisting of species mass, momentum, total energy, and vibrational–electron–electronic energy conservation equations.

In this study, the idea of elemental species conservation equation is introduced.[13] For high-temperature airflow, we employ the following 11 chemical species: N, O, N_2, O_2, NO, N^+, O^+, N_2^+, O_2^+, NO^+, and e^-. Moreover, we consider 10 species, C, C_2, C_3, CO, CN, C^+, H, H_2, C_2H, and H^+, as the ablation products from the heatshield of MUSES-C reentry capsule that is made of carbon–phenolic. The conservative variable $\boldsymbol{Q}$ thus becomes

$$\boldsymbol{Q} = (\tilde{\rho}_{\mathrm{N}}, \tilde{\rho}_{\mathrm{O}}, \tilde{\rho}_{\mathrm{C}}, \tilde{\rho}_{\mathrm{H}}, \rho_{\mathrm{N}}, \rho_{\mathrm{O}}, \rho_{\mathrm{NO}}, \rho_{\mathrm{N^+}}, \rho_{\mathrm{O^+}}, \rho_{N_2^+}, \rho_{\mathrm{O_2^+}}, \rho_{\mathrm{NO^+}},$$
$$\rho_{\mathrm{C}}, \rho_{\mathrm{CN}}, \rho_{\mathrm{CO}}, \rho_{\mathrm{C_3}}, \rho_{\mathrm{C^+}}, \rho_{\mathrm{H}}, \rho_{\mathrm{C_2H}}, \rho_{\mathrm{H^+}}, \rho u, \rho v, E, E_v)^t \qquad (1)$$

where a charge neutrality is assumed to omit ρ_{e^-}. Instead of solving the conservation equations for N_2, O_2, C_2, and H_2, the following relations are used to derive $\rho_{\mathrm{N_2}}$, $\rho_{\mathrm{O_2}}$, $\rho_{\mathrm{C_2}}$, and $\rho_{\mathrm{H_2}}$:

$$\frac{\tilde{\rho}_{\mathrm{N}}}{M_{\mathrm{N}}} = \frac{\rho_{\mathrm{N}}}{M_{\mathrm{N}}} + 2\frac{\rho_{\mathrm{N_2}}}{M_{\mathrm{N_2}}} + \frac{\rho_{\mathrm{NO}}}{M_{\mathrm{NO}}} + \frac{\rho_{\mathrm{N^+}}}{M_{\mathrm{N^+}}} + 2\frac{\rho_{\mathrm{N_2^+}}}{M_{\mathrm{N_2^+}}} + \frac{\rho_{\mathrm{NO^+}}}{M_{\mathrm{NO^+}}} + \frac{\rho_{\mathrm{CN}}}{M_{\mathrm{CN}}} \qquad (2a)$$

$$\frac{\tilde{\rho}_{\mathrm{O}}}{M_{\mathrm{O}}} = \frac{\rho_{\mathrm{O}}}{M_{\mathrm{O}}} + 2\frac{\rho_{\mathrm{O_2}}}{M_{\mathrm{O_2}}} + \frac{\rho_{\mathrm{NO}}}{M_{\mathrm{NO}}} + \frac{\rho_{\mathrm{O^+}}}{M_{\mathrm{O^+}}} + 2\frac{\rho_{\mathrm{O_2^+}}}{M_{\mathrm{O_2^+}}} + \frac{\rho_{\mathrm{NO^+}}}{M_{\mathrm{NO^+}}} + \frac{\rho_{\mathrm{CO}}}{M_{\mathrm{CO}}} \qquad (2b)$$

$$\frac{\tilde{\rho}_{\mathrm{C}}}{M_{\mathrm{C}}} = \frac{\rho_{\mathrm{C}}}{M_{\mathrm{C}}} + 2\frac{\rho_{\mathrm{C_2}}}{M_{\mathrm{C_2}}} + \frac{\rho_{\mathrm{CN}}}{M_{\mathrm{CN}}} + \frac{\rho_{\mathrm{CO}}}{M_{\mathrm{CO}}} + 3\frac{\rho_{\mathrm{C_3}}}{M_{\mathrm{C_3}}} + \frac{\rho_{\mathrm{C^+}}}{M_{\mathrm{C^+}}} + 2\frac{\rho_{\mathrm{C_2H}}}{M_{\mathrm{C_2H}}} \qquad (2c)$$

$$\frac{\tilde{\rho}_{\mathrm{H}}}{M_{\mathrm{H}}} = \frac{\rho_{\mathrm{H}}}{M_{\mathrm{H}}} + 2\frac{\rho_{\mathrm{H_2}}}{M_{\mathrm{H_2}}} + \frac{\rho_{\mathrm{C_2H}}}{M_{\mathrm{C_2H}}} + \frac{\rho_{\mathrm{H^+}}}{M_{\mathrm{H^+}}} \qquad (2d)$$

The total density is given by a sum of these elemental densities.

The governing equations for elemental densities $\tilde{\rho}_{\mathrm{N}}$, $\tilde{\rho}_{\mathrm{O}}$, $\tilde{\rho}_{\mathrm{C}}$, and $\tilde{\rho}_{\mathrm{H}}$ can be written in the form of convection equation as[13]

$$\frac{\partial \tilde{\rho}_s}{\partial t} + \frac{\partial \tilde{\rho}_s u}{\partial x} + \frac{\partial \tilde{\rho}_s v}{\partial y} + \frac{\tilde{\rho}_s v}{y} = 0, \qquad s = \mathrm{N, O, C, H} \qquad (3)$$

for the axisymmetric flowfield. Note that there is no source term in Eq. (3) because chemical reactions preserve the elements. Note that the diffusion term in the elemental density conservation equation is omitted. This implies that the diffusion term of the removed chemical species is so determined that the overall diffusion of the corresponding element is to be vanished. In this respect, the use of an elemental density conservation equation of the present form is less rigorous. Nevertheless, we have employed it because it seems a reasonable compromise that can satisfy conservation of total mass and numerical robustness of the scheme simultaneously. Note that the diffusion effects of those atomic species that contribute to the surface reactions and, hence, to the wall heating rate are all retained in the species conservation equations. In Ref. 13, the advantages of using elemental density conservation equations in conjunction with the diagonal implicit scheme[14] indicate that 1) elements are always conserved no matter how the remaining chemical species evolve during convergence to steady state and 2) the evolution of the total density conservation equation is not lagged behind those of momentum and total energy equations.

Park's two-temperature model is employed to describe the nonequilibrium thermochemical states. The vibrational–electron–electronic energy conservation equation accounts for 1) vibrational energy excitation of molecules through collisions between heavy particles, 2) elastic energy transfer between electrons and heavy particles, 3) gains or losses of energy by electron impact ionization, and 4) gains or losses of vibrational–electron–electronic excitation energy of heavy particles in chemical reactions.[15] The preferential dissociation model is not used in this study. Vibrational relaxation parameters, such as a vibrational relaxation time, are taken from Refs. 16 and 17. The relaxation time is accounted for Park's limiting cross section at high temperature. The values of reaction rate coefficients are taken from Refs. 16 and 18.

The governing equations are integrated by a finite volume method. The numerical flux at a cell interface is provided by the AUSM-DV upwind scheme.[19] Spatial accuracy is improved by the MUSCL approach. An explicit method is used for the time integration, and the diagonal point implicit method[14] is employed for stability maintenance of the source term. Use of the elemental density conservation equation somewhat complicates the derivation of the Jacobian matrix for the point implicit method but can reduce the number of species conservation equations that contain chemical source term. A local time stepping method is used for a faster convergence.

Calculation of Radiative Heat Flux

The radiative heat flux at the wall surface is computed from the obtained flowfield data using the tangent-slab approximation. The emission and absorption coefficients are first calculated using a multiband model. In the present multiband model, the absorption coefficients are evaluated at 2294 wavelength points for air and at 7610 wavelength points for carbonaceous and hydrogenic species. They are constructed for the wavelength region from 750 to 15,000 Å. The absorption coefficient of the gas mixture is expressed as a sum of those for individual species in the form of[20]

$$\kappa_\lambda = \sum_i n_i \sigma_{\lambda_i} \tag{4}$$

The cross section value is curve fitted using the five parameters in the form of

$$\sigma_{\lambda_i} = \exp\left(A^i_{\lambda_1}/z + A^i_{\lambda 2} + A^i_{\lambda 3} \ln z + A^i_{\lambda 4} z + A^i_{\lambda 5} z^2\right) \tag{5}$$

where $z = 10{,}000/T_v$.

Material Thermal Response Code and Surface Reactions

When one tries to obtain the net heating rate at a wall with ablation, consistent boundary conditions between a CFD and a CMA code should be specified at least in a loosely coupled manner. In the CMA code, four conservation equations, that is, conservation of solid density, pyrolysis gas density, momentum of pyrolysis gas, and energy equations, are solved one dimensionally.[9] Because the phenomenon of ablation is essentially time dependent, these equations are solved along the flight trajectory by changing the boundary conditions, such as heating rates. The convective heating rate and the radiative heating rate at the wall at a specified time is provided from the CFD solution. The heating rate at intermediate time is interpolated.

The surface of the carbon–phenolic ablator becomes a char layer under severe aerodynamic heating. The material response properties, such as an emissivity and densities of virgin and char layers, are taken from Ref. 21.

The injection rate of pyrolysis gas from the wall is given by the CMA code as

$$\dot{m}_P = \varepsilon \rho_P u_P \tag{6}$$

The void fraction represents the degree of porosity. Pyrolysis gas passes through these voids. Because the CMA code solves the void fraction one dimensionally to the wall surface, we assume the porosity at the wall surface is identical with the void fraction. Therefore, at the wall, the ratio of the void portion and the catalytic wall mostly consisting of char is given by $\varepsilon : 1 - \varepsilon$. The solid and the pyrolysis gas are assumed to be at the same temperature, and the surface composition of the pyrolysis gas is assumed to be in chemical equilibrium at the common temperature and pressure.

The surface reactions used in this study are described in detail in Ref. 18. The surface reaction velocity is given by kinetic theory as

$$k_{wi} = \alpha_i \sqrt{8kT_w/\pi M_s}\Big/4 \tag{7}$$

The reaction rates are given by

$$J_i = (\rho \gamma_s k_{wi})_w \tag{8}$$

We consider the following four types of chemical reactions that occur at the ablator surface.

1) The surface oxidation:

$$\mathrm{O} + \mathrm{C}(s) \rightarrow \mathrm{CO} \tag{9}$$

$$\alpha_1 = 0.63 \exp(-1160/T_w), \qquad M_s = M_\mathrm{O}, \qquad J_1 = (\rho \gamma_\mathrm{O} k_{w1})_w \tag{10}$$

where $\mathrm{C}(s)$ is the carbon atom of the solid surface.

2) The surface nitridation:

$$\mathrm{N} + \mathrm{C}(s) \rightarrow \mathrm{CN} \tag{11}$$

$$\alpha_2 = 1, \qquad M_s = M_\mathrm{N}, \qquad J_2 = (\rho \gamma_\mathrm{N} k_{w2})_w \tag{12}$$

3) The surface sublimation:

$$\mathrm{C}(s) \rightarrow \mathrm{C}_3 \tag{13}$$

$$\alpha_3 = 30 \exp(-21{,}490/T_w), \qquad M_s = M_{\mathrm{C}_3}$$

$$J_3 = \lfloor \rho(\gamma_{E,\mathrm{C}_3} - \gamma_{\mathrm{C}_3}) k_{w3} \rfloor_w \tag{14}$$

We assume Eq. (13) because the sublimation product of graphite consists mostly of C_3 (Ref. 18). The equilibrium composition of C_3 for the present study can be expressed as

$$\gamma_{E,\mathrm{C}_3} = 1.9 \times 10^9 \exp(-59{,}410/T_w)/(\rho_w T_w) \tag{15}$$

4) The recombination of ions and electrons:

$$A^+ + e^- \rightarrow A \quad (A : \text{ions}) \tag{16}$$

$$\alpha_n = 1, \qquad M_s = M_A, \qquad J_n = (\rho \gamma_{A^+} k_w)_w \tag{17}$$

The catalytic recombination processes such as

$$2\mathrm{N} \rightarrow \mathrm{N}_2, \qquad 2\mathrm{O} \rightarrow \mathrm{O}_2 \tag{18}$$

are ignored. The concentration of surface reacting species can be found by solving the relations that the production rate at the wall balances with diffusion.

Turbulence Model

The turbulence model and concept of injection-induced turbulence used in this study are described in detail in Ref. 7. The injection-induced turbulence model was implemented into CFD code by the following approach: We describe the eddy viscosity as

$$\mu_t = (\mu_t)_\mathrm{BL} + (\mu_t)_\mathrm{inj} \tag{19}$$

where the first term in the right-hand side is given by the original form of the Baldwin–Lomax turbulence model.[22] The second term is given by

$$(\mu_t)_\mathrm{inj} = \rho d^2 |\omega| \tag{20}$$

$$d = \max(0, d_w - \chi y) \exp(-y^+/A^+) \tag{21}$$

The mixing length d takes the maximum value d_w at the wall and decays exponentially in the boundary layer according to the Van Driest theory. The wall mixing length d_w is chosen to satisfy the relation

$$\left(\mu_{t_w}\right)_\mathrm{Park} = \rho_w d_w^2 |\omega|_w \tag{22}$$

Code Validation

Because the present unified code consists of several computer codes that have been separately developed, let us describe a brief validation history of the software. The thermochemical package used in the CFD code was originally developed for airflows accounting for five neutral air species. Verification was attempted to reproduce the Fay–Riddell correlation, and validation was made by reproducing the flight data of heat flux at the space shuttle nose.[23] It has also been checked extensively in the series of calculation of shock layer thickness over a sphere and cones in the intermediate hypersonic range.[24,25] The package was then extended to include carbonaceous species and applied to solve the entry flowfield of the Pioneer-Venus probe vehicle.[8]

The CMA code first reported by Ahn et al. was validated by the comparison with the experimental data obtained in arc heated airflow and was applied to solve the thermal response of ablator heatshield for the Pioneer-Venus probe vehicle.[9] The CMA code was also examined in detail in Ref. 26 for the ablator material of MUSES-C. The present study employs the same subroutine package that was used in Ref. 26.

The injection-induced turbulence model was first incorporated into a CFD code by combining with one-equation turbulence model. The code was applied to solve the velocity profile in the boundary layer over a spherical blunt body with foreign gas injection through a porous wall.[27] A peculiar velocity profile seen in the experiment was qualitatively reproduced. In another study, as stated in Introduction, the heating environment of the Pioneer-Venus probe vehicle with ablation was calculated.[6] The higher heating rate at the frustum edge observed in the flight data was also qualitatively reproduced. In Ref. 7, an alternative approach was studied in which the injection-induced turbulence model was combined with zero-equation algebraic turbulence model. This new scheme successfully reproduced the heat transfer rate at the stagnation point of a blunt body with foreign gas injection in the hypersonic flowfield. Though the heating rate in the downstream region was overestimated by factor of 2, the overall agreement with the experimental data was judged fair. With use of this new scheme, the entry flowfield of the Pioneer-Venus probe vehicle with ablation along the trajectory was calculated by the integrated CFD–CMA code.[8] A reasonable agreement with the flight data was obtained for the temperature history not only at the stagnation point but also at the frustum edge. The present unified code originates from this integrated CFD–CMA code.

Results and Discussion

The surface geometry for the MUSES-C reentry capsule is shown in Fig. 1. The forebody is a 45-deg sphere–cone with a nose radius of 0.2 m. Figure 2 shows a typical example of structured mesh with 59 × 77 grid points. The forebody computational domain extends to the shoulder. Figure 3 shows the reentry trajectory of the MUSES-C capsule with the chosen trajectory points denoted by circles where CFD calculations were made. The freestream conditions at these points are listed in Table 1. The entry angle into the atmosphere at 200 km is assumed as −12 deg.

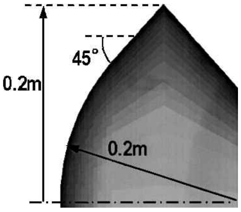

Fig. 1 Geometry of the MUSES-C reentry capsule.

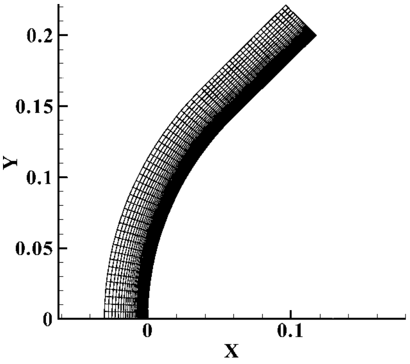

Fig. 2 Computational mesh with 59 × 77 grid points.

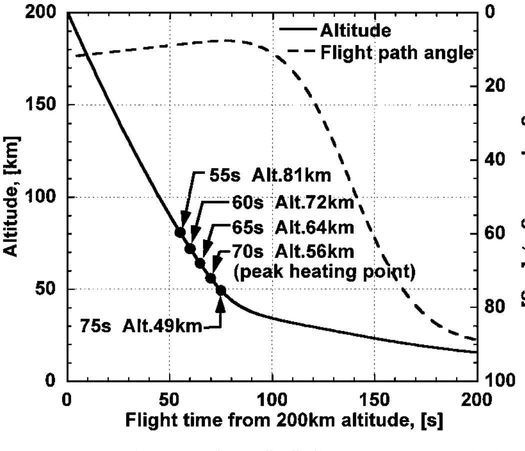

Fig. 3 Reentry trajectory of MUSES-C; entry angle at 200 km is assumed to be − 12 deg.

Table 1 Freestream flow conditions

Flight time, s	Altitude, km	Relative velocity, km/s	Density, kg/m^3	Temperature, K
55	81	12.053	$1.592e^{-5}$	215
60	72	11.947	$6.068e^{-5}$	220
65	64	11.600	$1.600e^{-4}$	230
70	56	10.611	$5.142e^{-4}$	245
75	49	8.870	$1.128e^{-3}$	255

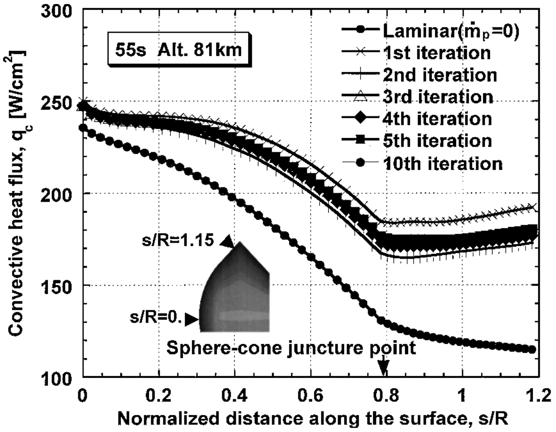

Fig. 4 Convergence history of the convective heat flux profile along the surface with ablation at 55 s from 200 km.

In the course of the present calculation, we first obtain an initial solution at the first trajectory point at 55 s of flight time. We assume that ablation and wall reactions are absent and that the boundary layer is laminar (hereafter called the laminar solution). The constant wall temperature is arbitrarily chosen as 3000 K. From this initial solution, we can find the boundary conditions for the CMA code such as convective and radiative heat transfer rates. We assume the heat transfer rate is zero before 30 s (density is below 1.0×10^{-7} kg/m^3) and is interpolated by a quadratic function up to the first trajectory point at 55 s. With the interpolated heating rate during this period, the CMA code solves the thermal response of the ablator along the trajectory and gives the wall boundary condition such as wall temperature and injection rate from 30 to 55 s. Once the wall boundary condition at 55 s is specified, the new CFD solution with the ablation effect is calculated at the same trajectory point. The converged solution then gives the new boundary condition for the CMA code at 55 s, and the thermal response of ablator is again calculated along the trajectory. In this way, the CFD code and the CMA code are loosely coupled.

Figure 4 shows the convergence history of convective heat flux profiles along the wall surface at 55 s. As can be seen, although a small fluctuation still remains at larger normalized distances, convergence is virtually attained within 5 iterations if compared with the solution of the 10th iteration (hereafter the converged solution is called the turbulent solution). Note that the converged profile is substantially different from the initial one particularly in the downstream region due to turbulence effects. One can see a small spike in the heat flux profile at the stagnation point. This is a typical numerical error that often appears in the calculation when assuming an axisymmetric flowfield. Experience indicates that this spike can be eliminated if the detached shock wave is accurately resolved using a solution adaptive mesh system. Such an effort is not attempted in this study because the spike can only have a minor effect for overall heat flux profile. Figure 5 shows the radiative heat fluxes along the stagnation streamline. Both the wallward radiative heat flux component that finally reaches the wall surface as well as the shockward

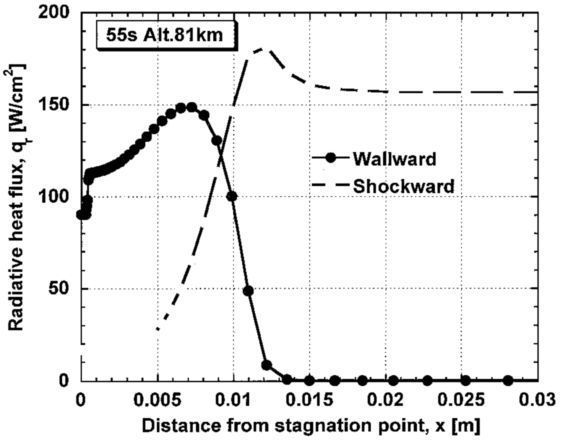

Fig. 5 Radiative heat flux components along the stagnation streamline at 55 s from 200 km.

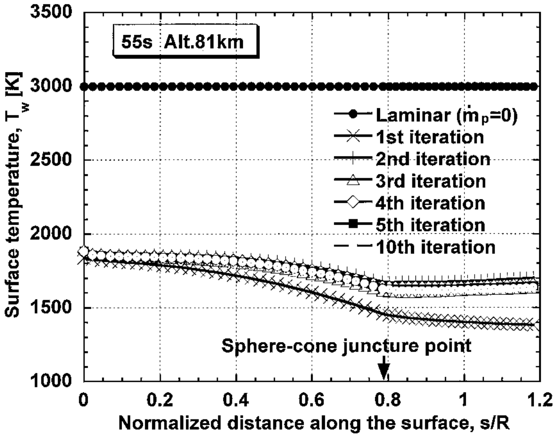

Fig. 6 Convergence history of wall temperature profile along the surface at 55 s from 200 km.

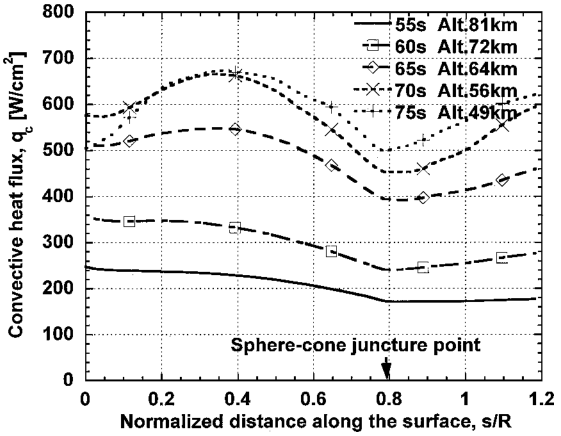

Fig. 7 Converged profile of the convective heat flux along the surface at the chosen trajectory points.

component that ultimately escapes from the computational domain are shown. The convergence history of the wall temperature profile is shown in Fig. 6.

Next, the CFD solution at 60 s of flight time is obtained. As before, we assume the initial flowfield to be laminar and without ablation. We then linearly interpolate the heat flux value from 55 to 60 s, which is fed into the CMA code. The solution from the CMA code then gives the new boundary condition for the CFD code. The converged and consistent solution accounting for ablation at 60 s is finally obtained iteratively. The converged solutions at 65, 70, and 75 s of flight time are similarly obtained by using the CFD solution at the previous trajectory point as the initial solution. Figure 7 shows

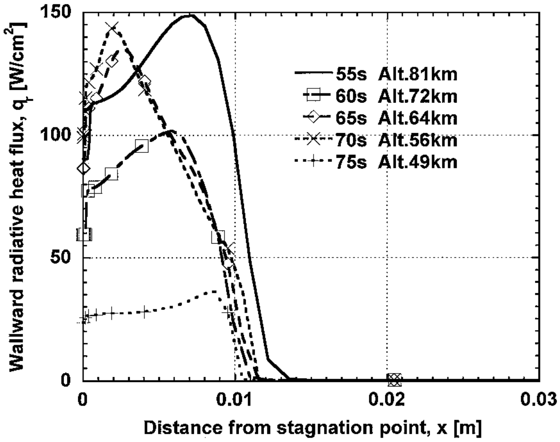

Fig. 8 Wallward radiative heat flux along the stagnation streamline at the chosen trajectory points.

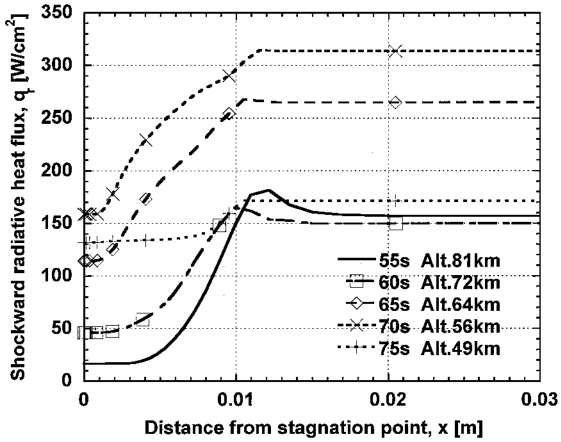

Fig. 9 Shockward radiative heat flux along the stagnation streamline at the chosen trajectory points.

the surface heating profiles accounting for ablation and turbulence at the chosen trajectory points. Because of the turbulent heating, the heating rate in the downstream region becomes larger particularly at 70 and 75 s of flight time. Moreover, because of the blockage effect due to the significant ablation, the heating rate at the stagnation point at 75 s is lower than that at 70 s. The computed wallward and shockward radiative heat fluxes along the stagnation streamline at those five trajectory points are compared in Figs. 8 and 9, respectively. It is indicated in Fig. 8 that the radiative heating along the stagnation streamline toward the wall at 55 s of flight time at the altitude of 81 km becomes larger than that at the lower altitude. This is because the vibration–electron–electronic temperature that dictates radiative heating rate in the two-temperature model becomes higher in the shock layer, as shown in Fig. 10.

Figure 11 shows the stagnation point heat transfer rates with ablation along the trajectory. The total heat flux at the stagnation point is defined here as a sum of the convective heat flux and the wallward radiative heat flux minus the shockward radiative heat flux. A maximum convective heat flux value of about 700 W/cm^2 is obtained at 70 s. After that time, the convective heat flux decreases because of the significant convective blockage effect. The wallward radiative heat flux is about 15% of the convective heat flux at the peak heating point.

The calculated temperature histories at the ablator surface are shown in Fig. 12. To compare directly with the existing result, the initial temperature of the ablator surface at altitude of 200 km is assumed as 300 K. At the stagnation region, the temperature history shows a fair agreement with that given by Suzuki et al.[28] They studied the stagnation heating and the ablation process of the MUSES-C capsule by using the laminar viscous shock layer (VSL) equations.

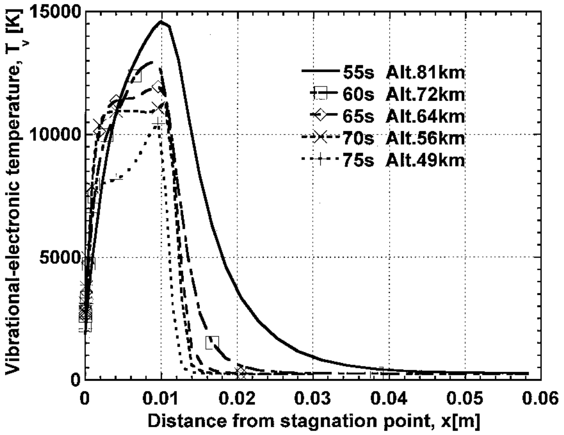

Fig. 10 Vibrational–electron–electronic temperature along the stagnation streamline at the chosen trajectory points.

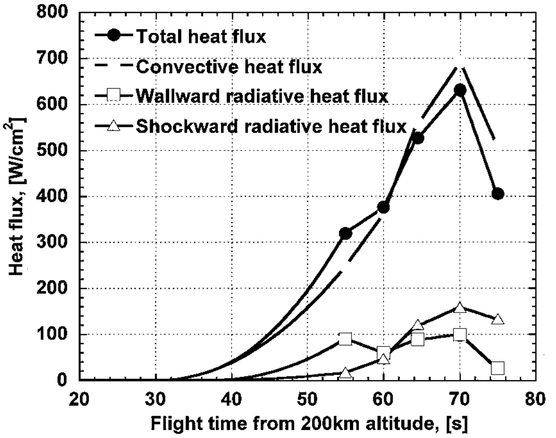

Fig. 11 Heat flux history at the stagnation point.

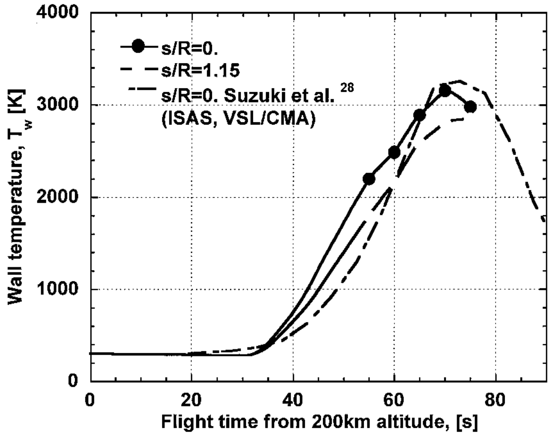

Fig. 12 Wall temperature history at the stagnation point and in the downstream region of the MUSES-C reentry capsule.

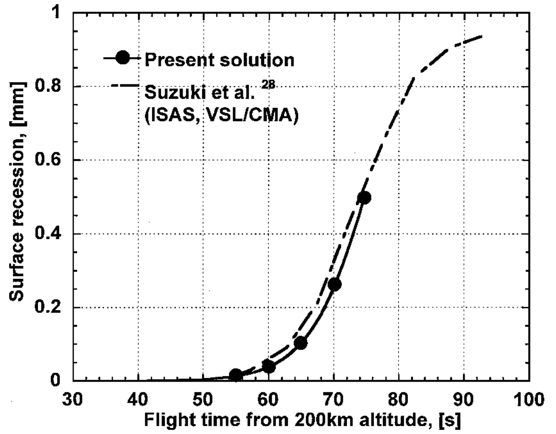

Fig. 13 Computed surface recession at the stagnation pont.

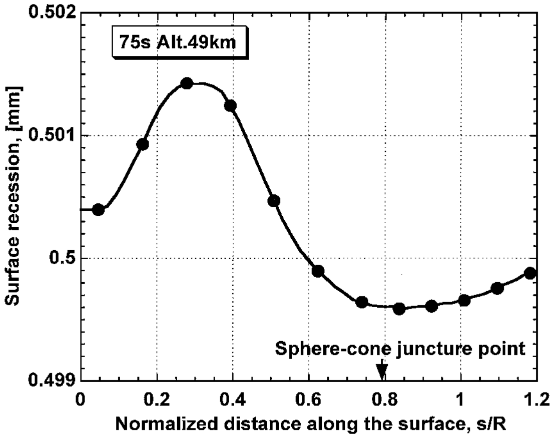

Fig. 14 Computed surface recession along the surface at 75 s from 200 km.

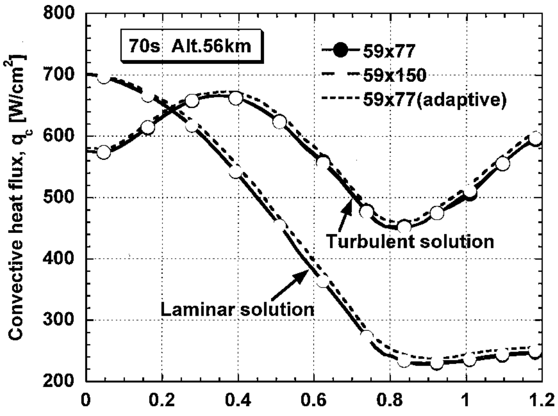

Fig. 15 Convective heat flux profiles at 70 s from 200 km obtained in the grid convergence study. Converged solution using an adaptive mesh also shown.

Although Suzuki et al. considered the laminar boundary layer with ablation, the heating rate became comparable with the present turbulent solution due to inclusion of catalytic recombination of O and N atoms. At the frustum edge, the higher heating can be seen because of the turbulence due to ablation product gas.

Figure 13 shows the surface recession at the stagnation point. Although the present solution is slightly shifted from that given in Ref. 28, the agreement between these solutions is fairly good. The calculated recession profile along the wall surface at 75 s of flight time is shown in Fig. 14. Because of significant turbulent heating in the downstream region, the surface recession becomes larger at $s/R = 0.3$ than that at the stagnation point and then gradually decreases toward the juncture point but slightly increases again at the frustum edge.

Finally, the results of grid convergence study are shown in Fig. 15. Both the laminar and the turbulent solutions at 70 s of flight time are examined. As can be seen, the calculated solutions using a finer mesh with 59 × 150 mesh points duplicate well the present solutions using the standard mesh that has 59 × 77 mesh points. In Fig. 15, the effect of mesh adaptation to the detached shock wave is also shown. Although a slight increase of heat flux value over the surface occurs for this case, the overall heat flux profile is seen to be unchanged.

Conclusions

A trajectory-based unified analysis on the aerodynamic heating environment for the MUSES-C reentry capsule is conducted by means of integrating a thermochemical nonequilibrium CFD code that accounts for 21 chemical species including carbonaceous ones, a CMA code that gives the thermal response of ablative heatshield, and an injection-induced turbulence model that characterizes the eddy viscosity of the ablation product gas. The radiative heat flux is computed by using the tangent-slab approximation with the multiband model and is used as the boundary condition in the CMA code, although calculation of the fully coupled flowfield with radiative heat transfer is not accomplished. Moreover, accounting for shape change due to recession in the CFD calculation and accounting for spalled particles from heatshield are as yet to be done. It is shown that the converged solution along the reentry trajectory can be obtained by loosely coupling the CFD code and the CMA code. The convergence at each trajectory point is reached within a few iterations. The maximum convective heat flux at the stagnation point is found to be about 700 $\mathrm{W/cm^2}$, whereas the wallward radiative heat flux becomes about 15% of the convective value at the peak heating point. It is also found that the wall temperature in the downstream frustum region is significantly elevated by the effect of turbulence due to the ablation product gas. The wall temperature, as well as the recession rate at the stagnation point along the entry trajectory, duplicates well that given by the existing VSL/CMA coupling calculation, although the existing result accounts for catalytic recombination of atomic oxygen and nitrogen at the wall surface, whereas the present study assumes a noncatalytic wall for those recombination reactions but includes the turbulence effect of the ablation product gas.

References

[1] Wakefield, R. M., and Pitts, W. C., "Analysis of the Heat-Shield Experiment on the Pioneer-Venus Entry Probes," AIAA Paper 80-1494, July 1980.

[2] Milos, F. S., "Galileo Probe Heat Shield Ablation Experiment," AIAA Paper 96-1823, June 1996.

[3] Park, C., "Heatshielding Problems of Planetary Entry, A Review," AIAA Paper 99-3415, July 1999.

[4] Milos, F. S., Chen, Y.-K., and Squire, T. H., "Analysis of Galileo Probe Heatshield Ablation and Temperature Data," *Journal of Spacecraft and Rockets*, Vol. 36, No. 3, 1999, pp. 298–306.

[5] Park, C., "Injection-Induced Turbulence in Stagnation Point Boundary Layers," *AIAA Journal*, Vol. 22, No. 2, 1984, pp. 219–225.

[6] Ahn, H.-K., Sawada, K., and Park, C., "CFD Calculation of Heat Fluxes in Turbulent Flow for Pioneer-Venus Probes," AIAA Paper 98-0833, Jan. 1998.

[7] Izawa, Y., and Sawada, K., "Calculation of Surface Heat Transfer for a Sphere with Wall Injection," *Journal of Thermophysics and Heat Transfer*, Vol. 14, No. 2, 2000, pp. 230–236.

[8] Izawa, Y., and Sawada, K., "Calculation of Hypersonic Flow with Ablation for Pioneer-Venus Probe," AIAA Paper 2000-0208, Jan. 2000.

[9] Ahn, H.-K., Park, C., and Sawada, K., "Dynamics of Pyrolysis Gas in Charring Materials Ablation," AIAA Paper 98-0165, Jan. 1998.

[10] Sakai, T., Sawada, K., and Park, C., "Assessment of Planck–Rosseland–Gray Model for Radiating Shock Layer," AIAA Paper 97-2560, June 1997.

[11] Tsuru, T., and Sawada, K., "Convergence Issues on Fully Coupled Radiative Gas Dynamic Calculations," AIAA Paper 2000-0732, Jan. 2000.

[12] Sakai, T., and Sawada, K., "Calculation of Nonequilibrium Radiation from a Blunt-Body Shock Layer," *Journal of Thermophysics and Heat Transfer*, Vol. 15, No. 1, 2001, pp. 99–105.

[13] Hassan, B., Candler, G. V., and Olynick, D. R., "The Effect of Thermochemical Nonequilibrium on the Aerobraking Vehicles," AIAA Paper 92-2877, July 1992.

[14] Eberhardt, S., and Imlay, S., "Diagonal Implicit Scheme for Computing Flow with Finite Rate Chemistry," *Journal of Thermophysics and Heat Transfer*, Vol. 6, No. 2, 1992, pp. 208–216.

[15] Park, C., *Nonequilibrium Hypersonic Aerothermodynamics*, Wiley, New York, 1989, pp. 124–129.

[16] Park, C., "Review of Chemical–Kinetic Problems of Future NASA Missions, Part 1: Earth Entries," *Journal of Thermophysics and Heat Transfer*, Vol. 7, No. 3, 1993, pp. 385–398.

[17] Park, C., Howe, J. T., Jaffe, R. L., and Candler, G. V., "Review of Chemical–Kinetic Problems of Future NASA Missions, Part 2: Mars Entries," *Journal of Thermophysics and Heat Transfer*, Vol. 8, No. 1, 1994, pp. 9–23.

[18] Park, C., Jaffe, R. L., and Partridge, H., "Chemical–Kinetic Parameters of Hyperbolic Earth Entry," *Journal of Thermophysics and Heat Transfer*, Vol. 15, No. 1, 2001, pp. 76–90.

[19] Wada, Y., and Liou, M. S., "A Flux Splitting Scheme with High-Resolution and Robustness for Discontinues," NASA TM 106452, 1994; also AIAA Paper 94-0083, Jan. 1994.

[20] Park, C., and Milos, F. S., "Computational Equations for Radiating and Ablating Shock Layers," AIAA Paper 90-0356, Jan. 1990.

[21] Working Group of Asteroid Sample Return Mission, "MUSES-C Mission Plan Report," Inst. of Space and Astronautical Science, Sagamihara, Japan, March 2000 (in Japanese).

[22] Baldwin, B. S., and Lomax, H., "Thin Layer Approximation and Algebraic Model for Separated Turbulent Flows," AIAA Paper 78-257, Jan. 1978.

[23] Niizuma, K., and Sawada, K., "Nonequilibrium Flow Computation for the Space Shuttle Nose Using Unstructured Meshes," AIAA Paper 97-2548, June 1997.

[24] Furudate, M., Nonaka, S., and Sawada, K., "Behavior of Two-Temperature Model in Intermediate Hypersonic Regime," *Journal of Thermophysics and Heat Transfer*, Vol. 13, No. 4, 1999, pp. 424–430.

[25] Furudate, M., Nonaka, S., and Sawada, K., "Calculation of Shock Shapes over Simple Geometry in Intermediate Hypersonic Air Flow," AIAA Paper 99-3686, June–July 1999.

[26] Ahn, H.-K., "Heatshield Problems of Pioneer-Venus and MUSES-C," Ph.D. Dissertation, Dept. of Aeronautics and Space Engineering, Tohoku Univ., Sendai, Japan, March 1998.

[27] Dendou, E., and Sawada, K., "Numerical Simulation of Hypersonic Flow over a Sphere with Surface Injection," AIAA Paper 98-0773, Jan. 1998.

[28] Suzuki, K., Fujita, K., and Abe, T., "Trajectory-Based Coupled Analysis of Viscous Shock-Layer and Charring Ablator for Stagnation Heating Environment of MUSES-C Re-Entry Capsule," *Symposium on Flight Mechanics and Astrodynamics*, Inst. of Space and Astronautical Science, Sagamihara, Japan, 1998, pp. 117–120 (in Japanese).